New Ab Initio Based Pair Potential for Accurate Simulation of Phase Transitions in ZnO

Shuaiwei Wang,[†] Zhaochuan Fan,[‡] Rik S. Koster,[§] Changming Fang,[§] Marijn A. van Huis,[§]
Anil O. Yalcin,[‖] Frans D. Tichelaar,[‖] Henny W. Zandbergen,[‖] and Thijs J. H. Vlugt*[,‡]

[†]Institute of Nanostructured Functional Materials, Huanghe Science and Technology College, Zhengzhou Henan 450006, China

[‡]Process and Energy Department, Delft University of Technology, Leeghwaterstraat 39, 2628 CB Delft, The Netherlands

[§]Soft Condensed Matter, Debye Institute for Nanomaterials Science, Utrecht University, Princetonplein 5, 3584 CC Utrecht, The Netherlands

[‖]Kavli Institute of Nanoscience, Delft University of Technology, Lorentzweg 1, 2628 CJ Delft, The Netherlands

Ⓢ *Supporting Information*

ABSTRACT: A set of interatomic pair potentials is developed for ZnO based on the partially charged rigid ion model (PCRIM). The derivation of the potentials combines lattice inversion, empirical fitting, and ab initio energy surface fitting. We show that, despite the low number of parameters in this model (8), a wide range of physical properties is accurately reproduced using the new potential model. The calculated lattice parameters and elastic constants of ZnO in the wurtzite (WZ) phase, as well as the lattice parameters and stabilities of ZnO in other high-pressure and metastable phases, agree well with experiments and with density functional theory (DFT) calculations. The calculated transition pressure of the wurtzite-to-rocksalt (WZ-to-RS) transition is 12.3 GPa. A wurtzite-to-honeycomb (WZ-to-HC) phase transition induced by uniaxial pressure along the *c*-axis is simulated by means of molecular dynamics (MD) simulations. The WZ-to-HC transition takes place at an uniaxial pressure of 8.8 GPa while the reverse transition takes place at 2.9 GPa, which is consistent with DFT calculations. Other physical properties, including phonon dispersion, phonon density of states, and melting point calculated using our ZnO potential model are in good agreement with experimental and DFT data. Limitations of the novel ZnO potential model are also discussed.
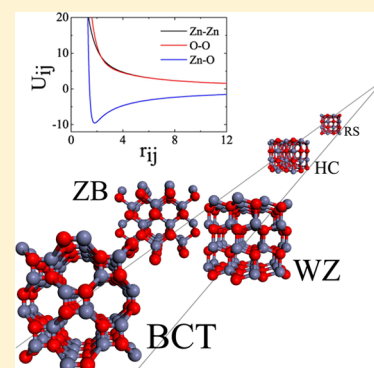
1. INTRODUCTION

Zinc oxide (ZnO) is a II−VI group semiconductor with a very wide range of applications, which covers the fields of rubber, ceramic and food industries, paint, pharmaceutics, and electronic devices.[1,2] The first use of ZnO can be traced back to thousands of years ago, and elaborate studies on ZnO materials have been carried out for more than seven decades.[1,2] In recent years, due to the development of the synthesis of low-dimensional ZnO and its potential application in optoelectronic devices,[1−6] the interest in ZnO has reached a new peak. In nature, ZnO is stable in the wurtzite (WZ) structure at ambient conditions. Many different methods have been developed to synthesize high-quality bulk and thin-film WZ−ZnO.[7−9] ZnO with the zinc blende (ZB) structure has a relatively higher cohesive energy compared to the WZ structure, which is therefore energetically unfavorable at zero temperature and zero pressure conditions.[10] The synthesis of ZB−ZnO can be achieved by growing thin films on specific substrates.[11,12] A pressure-induced wurtzite-to-rocksalt (WZ-to-RS) phase transition can be observed at a transition pressure of about 10 GPa.[13−16] A further RS-to-CsCl transition was predicted by DFT calculations at 260 GPa,[10] which has not yet been observed in experiments. ZnO nanostructures can be

synthesized with diverse morphologies, including nanoparticles and nanorods,[17,18] nanowires and nanobelts,[19,20] nanohelices,[21] nanorings and nanotubes,[22,23] nanomultipods and nano-flowers.[24−26] The diversity of the ZnO nanostructures enables the potential application of ZnO materials in transparent electronics, photodetecters, and solar cells, and for nanomotion and biosensing.[4−6,27]

Theoretical studies on ZnO have been mainly first-principles calculations[10,16,28−46] and molecular simulations using empirical or semiempirical potentials.[45,47−62] Density functional theory (DFT) calculations have been widely used for the studies of the physical properties of ZnO, including the crystal structures and mechanical properties,[10,28,29] electronic structure,[30,31] vibrational properties,[16,32−34] structural stability, and phase transitions.[10,28,32,35−43,46] Although proven to be accurate, DFT calculations were often restricted to static calculations and to small systems containing few atoms. Moreover, temperature effects were usually treated within the quasi-harmonic approximation, whereby anharmonicities were neglected.

Alternatively, using classical force fields, not only many physical properties can be studied easily by lattice statics (LS) and lattice dynamics (LD) simulations, but also temperature effects with full consideration of anharmonicities, and larger systems such as nanostructures consisting of thousands or even a few million atoms[60] can be studied by molecular dynamics (MD) or Monte Carlo (MC) simulations. However, the accuracy of MD or MC simulations directly depend on the accuracy of the potentials used.

There have been several attempts to develop interaction potentials for ZnO, including shell models (SM) by Lewis and Catlow[63] and by Binks et al.,[64] an analytic bond-order potential (ABOP) by Erhart et al.,[65] and a reactive force field (ReaxFF) by Raymand et al.[51,66] The SM derived by Binks et al.[64] is one of the most frequently used potential models for ZnO. This potential set reproduces several physical properties of ZnO in the WZ, ZB and RS structures with considerable accuracy. Unfortunately, it fails to precisely reproduce the stabilities of the intermediate states in the WZ-to-RS phase transition and the phonon dispersion curves of WZ−ZnO. The SM derived by Lewis and Catlow[63] yields a transition pressure of 3.7 GPa for the WZ-to-RS phase transition, which differs from the experimental one by about 60%. In 2002 and 2008, the same research group proposed a more complicated SM[57] for ZnO with piecewise functions and a modified version.[58] These new SMs accurately predicts several physical properties of ZnO polymorphs[59] as well as the stable and metastable structures of $(ZnO)_n$ ($n = 1-32$) clusters.[58] These SMs contain more than 30 parameters, whose functional forms are complex. Potentials with a very complex functional form may suffer from difficult fitting procedures[67,68] and possible inefficiencies in applications. Similar problems also exist in the ABOP[65] model (37 parameters) and the ReaxFF[66] model (93 parameters) for ZnO. Therefore, the development of a novel interatomic potential model for ZnO, which has a simple functional form and is accurate and computationally efficient, is important for simulation studies of ZnO and related materials.

The traditional procedure to develop empirical potentials is that the type of the potential is chosen first, and subsequently, the parameters are obtained by directly fitting to experimental data.[69] The potentials derived in this way obviously match some of the experimental results but are likely to be inaccurate in describing the physical properties of other high-pressure, metastable, or intermediate phases. Although many physical properties of these nonstable phases can be obtained by DFT calculations that can be used for fitting the potentials, the correctness of the potentials derived is not guaranteed directly from the first principles calculations since the parameters of potentials with respect to the same set of data are nonunique. In contrast to any of the fitting procedures, the lattice inversion (LI) method proposed by Chen[70] directly extracts the information on the interatomic interactions from the first principles calculations. By building multiplicative semigroups and using Möbius inversion, the LI derives the interatomic potentials in crystals from the energy lattice ($E-a$) curves calculated by DFT. The LI method has been successfully applied to the development of interaction potentials for metals,[71] rare earth elements,[72] alkali halides,[73] and semi-conductors.[74] The functional forms of the potentials do not need to be preselected in the LI method, but are chosen based on the shapes of the inverted potentials. Therefore, the potentials derived by the LI method incorporate intrinsic accuracy from first principles. However, the LI method has its

own limitations. Because three-body and many-body interactions are not taken into consideration and due to approximations made in the first-principles calculations, some physical properties calculated by the potentials directly derived by the LI method have a relatively large deviation with respect to experimental results.

In this work, we combine the LI method with an empirical and ab initio energy surface fitting procedure, and we developed a set of interatomic pair potentials for ZnO within the partially charged rigid ion model[75] (PCRIM) approach. We first used DFT calculations and the LI method to choose appropriate functional forms of the potentials to describe different interatomic interactions and to obtain the parameters. The parameter set was used as an initial guess in the next empirical and energy surfaces fitting procedure. The parameters for the ZnO potential model were adjusted by fitting them to reproduce the lattice parameters and relative energies of ZnO in the WZ, ZB, RS, and honeycomb (HC) structures as well as the elastic constants of WZ−ZnO. The potential model with the adjusted parameter set was examined by comparing with the initial guess to avoid any significant change after fitting. In this way, the correctness of the potential model is guaranteed by first-principles calculations, and the precision of the potential model is adjusted by fitting to experimental and DFT data. Our new ZnO potential model was validated by its ability to reproduce a variety of physical properties of ZnO in various structures. The "validation" set includes lattice parameters and structural stabilities of ZnO in the cesium chloride (CsCl) and the body-centered tetragonal (BCT) structures, high-temperature and high-pressure measurements, vibrational properties, and surface energies of WZ−ZnO. Our ZnO potential model only contains eight parameters and can be used in most of the current MD or MC codes, which enables molecular simulations to be flexible. The shortcomings of the ZnO potentials are also discussed to ensure appropriate use in the future.

2. DERIVATION OF POTENTIALS

2.1. Density Functional Theory Calculations. First principles density functional theory calculations were performed using the VASP code.[76] Within the projected augmented wave (PAW) method,[77] the generalized gradient approximation (GGA) functionals by Perdew, Burke, and Ernzerhof[78] (PBE) were used. The cutoff energy was set to a relatively high value of 600.0 eV, while the cutoff of the augmentation waves was set to 900.0 eV. Calculations were performed for six phases: WZ, RS, ZB, HC, CsCl, and BCT crystal structures. For the conventional unit cells of RS and ZB, a Monkhorst Pack k-mesh[79] of 24 × 24 × 24 was used, while for the CsCl and BCT structures, k-meshes of 40 × 40 × 40 and 21 × 21 × 35 were used, respectively. For the hexagonal WZ and HC structures, gamma centered k-point meshes of 30 × 30 × 26 and 30 × 30 × 30 respectively were used. A scan over cut off energies and k-point meshes show that the results are well converged within 0.5 meV/atom.

Bader charge analysis[80] unambiguously defines the effective charges on the atoms. Hereby the boundary between two atoms is defined by the surface at which the derivative of the charge density is equal to zero. The charge in the volume enclosed by that surface then determines the charge of the atoms. For this method, the Bader Charge Analysis code written by Arnaldsson et al.[81−83] was used. The results show that the Bader charges on the Zn atoms in the WZ, RS, ZB, HC, CsCl, and BCT structures are 1.22, 1.26, 1.23, 1.22, 1.12, and 1.22 electrons,

respectively. Differences between the Bader charges of different structures are small, in particular, between the ZB, WZ, HC, and BCT phases, which is in line with expectation since the ZB, HC, and BCT phases are structurally closely related to the WZ phase.

2.2. Lattice Inversion Method. The LI method has been described in detail in refs 70 and 73; here we only briefly present the essential steps of the LI method. Assuming that the interatomic interactions in a system contains only pair−body interactions, the total energy can be expressed as the sum of the pair potentials, $\varphi(x)$:

$$E(x) = \frac{1}{2} \sum_{n=1}^{\infty} r_0(n)\varphi(b_0(n)x) \tag{1}$$

where x is the nearest-neighbor atomic distance, $r_0(n)$ is the coordination number and $b_0(n)x$ is the atomic distance of the nth neighbor. To solve eq 1, a multiplicative semigroup $\{b(n)\}$ needs to be extended from the unclosed group $\{b_0(n)\}$ by multiplying any two elements in $\{b_0(n)\}$. Then eq 1 can be rewritten as

$$E(x) = \frac{1}{2} \sum_{n=1}^{\infty} r(n)\varphi(b(n)x) \tag{2}$$

where

$$r(n) = \begin{cases} r_0(b_0^{-1}(b(n))), & (b(n) \in b_o(n)) \\ 0, & (b(n) \notin b_o(n)) \end{cases} \tag{3}$$

Using the Möbius transformation, $\varphi(x)$ can be derived as

$$\varphi(x) = 2 \sum_{n=1}^{\infty} I(n)E(b(n)x) \tag{4}$$

where $I(n)$ is the inversion coefficient that is uniquely determined by the crystal geometrical structure.

Three structures (ZB, RS, and PbO−B10) were chosen to perform the total energy DFT calculations for ZnO. The lattice constant a varied from 3.0 to 12.0 Å. In this work, the PCRIM[75] was used to describe the atomic interactions in ZnO. The PCRIM is one of the simplest models in materials computation which has had great success in the computational studies of binary semiconductors.[84−87] In this model, the interatomic interaction only contains Coulombic interactions and short-range two-body interactions. The effective charges were initially selected as 1.2 e for our ZnO model based on the Bader analysis. The influence of the selection of the effective charges on the potential model will be discussed in more detail below. Once the effective charge had been determined, we used eqs 2−4 to invert the short-range pair potentials, $\phi(r_{ij})$. In the RS and ZB structures, both the cation and the anion sublattices are face-centered cubic. The cation sublattice and the anion sublattice have a relative displacement along the body diagonal of $(0.5,0.5,0.5)a$ in the RS structure and of $(0.25,0.25,0.25)a$ in the ZB structure, where a is the lattice parameter of the conventional unit cell. So the energy difference between the ZB and RS structures with the same lattice parameters only contains information about the Zn−O interaction. The cation sublattice in the PbO−B10 structure is the same as that in the ZB structure (fcc). The relative displacements of the nearest neighbor cations and anions are the same in PbO−B10 and ZB structures ($a/4$). Therefore, the energy difference between ZB and PbO−B10 only originates from the difference in the

anion−anion interactions in these two structures. The short-range interactions in ZnO can be obtained as follows:

$$\Delta E_{\text{short-range}}^{\text{RS-ZB}} = (E_{\text{total}}^{\text{RS}} - E_{\text{coul}}^{\text{RS}}) - (E_{\text{total}}^{\text{ZB}} - E_{\text{coul}}^{\text{ZB}}) \Rightarrow \phi_{+-}(r_{ij}) \tag{5}$$

$$\Delta E_{\text{short-range}}^{\text{ZB-PbO}} = (E_{\text{total}}^{\text{ZB}} - E_{\text{coul}}^{\text{ZB}}) - (E_{\text{total}}^{\text{PbO}} - E_{\text{coul}}^{\text{PbO}}) \Rightarrow \phi_{--}(r_{ij}) \tag{6}$$

$$\Delta E_{\text{short-range}}^{\text{ZB}} = E_{\text{total}}^{\text{ZB}} - E_{\text{coul}}^{\text{ZB}} - E_{+-}^{\text{ZB}} - E_{--}^{\text{ZB}} \Rightarrow \phi_{++}(r_{ij}) \tag{7}$$

where the subscripts, +−, −−, and ++ represent the cation−anion, anion−anion, and cation−cation interactions, respectively. E_{total} is the total energy and E_{coul} is the electrostatic energy (Madelung energy). Details of the derivation can be found in ref 74.

The upper-right inset in Figure 1 shows the data points of the inverted short-range interactions of ZnO. According to the
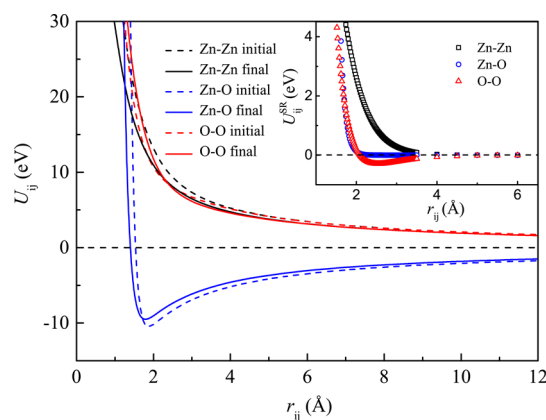
Figure 1. Interatomic pair potentials for ZnO. The dashed lines correspond to parameters obtained by the LI method (the initial guess), and the solid lines correspond to the parameters after fitting (final parameters). The upper-right inset shows the inverted short-range potentials before fitting.

inverted data points, the non-Coulombic interactions between Zn−O and Zn−Zn are mostly repulsive. Therefore, the potential in the Born-Mayer model[88] was chosen to describe the short-range Zn−O and Zn−Zn interactions:

$$\phi(r_{ij}) = Ae^{-r_{ij}/\rho} \tag{8}$$

The inverted data points of O−O non-Coulombic interaction shows a minimum at the atomic distance of 2.53 Å. The Morse type potential[89] was chosen to describe the short-range O−O interaction:

$$\phi(r_{ij}) = A[(1 - e^{-C(r_{ij}-\rho)})^2 - 1)] \tag{9}$$

All eight potential parameters were listed in Table 1. A cutoff radius of 12.0 Å was set for all short-range non-Coulombic interactions, and the Ewald method[90,91] was used to calculate the long-range Coulombic interactions in both real and reciprocal space.

Two issues should be discussed here. First, since the value of the effective charge is preselected by a Bader analysis before the LI, it is of interest to know how the inverted short-range potentials depend on the chosen effective charge. To investigate this, we repeated the LI procedure to derive the short-range cation−anion (Zn−O) interactions using different

Table 1. Parameters of the Interaction Potentials for ZnO from the LI Method (Initial Guess) and after Applying the Fitting Procedures (Final Parameters)[a]

			short-range interactions			effective charge
	interaction	type	A	ρ	C	q
initial guess	Zn–Zn	Born-Mayer[b]	111.6	0.5372		±1.2
	Zn–O	Born-Mayer[b]	7995000	0.1114		
	O–O	Morse[c]	0.2885	2.529	1.584	
final parameters	Zn–Zn	Born-Mayer[b]	78.91	0.5177		±1.14
	Zn–O	Born-Mayer[b]	257600	0.1396		
	O–O	Morse[c]	0.1567	3.405	1.164	

[a]A is in eV; ρ is in Å; C is in Å^{-1}; and the effective ion charges, q, is in e. [b]Eq 8 in text. [c]Eq 9 in text.

Table 2. Physical Properties of ZnO Calculated by LS and MD Simulations, Compared with Experimental Data, the Shell Model (SM), the Analytic Bond-Order Potential (ABOP), the Reactive Force Field (ReaxFF), and DFT Calculations[a]

		force fields				ab initio calculations	
	expt[b]	PCRIM, this work	SM[c]	ABOP[d]	ReaxFF[e]	this work	literature[f]
Wurtzite, Space Group $P6_3mc$ (No. 186)							
a	**3.242** (3.250)	{3.254} 3.238 (3.252)	3.271	3.219	3.29	3.287	3.199, 3.292
c	**5.188** (5.204)	{5.175} 5.176 (5.197)	5.138	5.257	5.3	5.306	5.162, 5.292
u	**0.3819**	{0.3823} 0.3814	0.3893	0.375		0.3790	0.3790, 0.3802
c_{11}	**222.6** (207)	{237.7} 221.2	232.5	212	222.9	185.8	226
c_{12}	**132.1** (117.7)	{140.8} 119.8	95.2	116	116.3	107.8	139
c_{13}	**122.0** (106.1)	{119.2} 97.2	85.6	109	103.5	94.2	123
c_{33}	**236.8** (209.5)	{221.3} 222.8	210.5	219	212.8	199.7	242
c_{44}	**47.5** (44.8)	{49.5} 51.2	74.6	43	57.1	36.5	40
c_{66}	**44.3** (44.65)	{48.4} 50.7	68.6	48		39.0	44
B	(136–183)	{160.8} 143.5	133.7	144	144	129.3	162.3, 133.7
Zinc Blende, Space Group $F\bar{4}3m$ (No. 216)							
a	(4.47, 4.595)	{4.564} 4.548	4.567	4.552	4.62	4.629 [**4.552**]	4.509, 4.633
$\Delta E_{ZB\text{-}WZ}$		{0.038} 0.034	0.09	0	0.042	**0.014**	0.015, 0.013
Rock Salt, Space Group $Fm\bar{3}m$ (No. 225)							
a	(4.271, 4.280)	{4.186} 4.262	4.32	4.275	4.44	4.337 [**4.265**]	4.229, 4.345
$\Delta E_{RS\text{-}WZ}$		{0.331} 0.306	0.283	0.237	0.335	**0.294**	0.158, 0.237, 0.31
Cesium Chloride, Space Group $Pm\bar{3}m$ (No. 221)							
a		{2.605} 2.691	2.662	2.642	2.64	2.691 [2.646]	2.624, 2.705
$\Delta E_{CsCl\text{-}WZ}$		{1.763} 1.816	1.92	0.976	1.63	1.434	1.307, 1.358
Honeycomb, Space Group $P6_3/mmc$ (No. 194)							
a		{3.484} 3.404	3.393			3.465 [**3.407**]	
c		{4.117} 4.489	4.634			4.580 [**4.504**]	
$\Delta E_{HC\text{-}WZ}$		{0.084} 0.165	0.091			**0.138**	0.16
Body-Centered Tetragonal, Space Group $P4_2/mnm$ (No. 136)							
a		{5.541} 5.482	5.539			5.624 [**5.531**]	5.48
c		{3.234} 3.256	3.232			3.285 [**3.231**]	3.17
u		{0.316} 0.320	0.317			0.319	
$\Delta E_{BCT\text{-}WZ}$		{−0.013} 0.056	0.007			0.048	0.074

[a]Lattice parameters a and c are in Å; u is the internal coordinate; the elastic constant c_{ij} and bulk modulus B are in GPa; energy difference ΔE is in eV/f.u. The values in parentheses are experimental or MD results at 300 K; the values in square brackets are normalized lattice parameters from DFT calculations (see main text); The values in the curly brackets are calculated with the initial guess (unmodified parameters); the values in bold are data used for fitting the force field parameters. [b]Experimental data measured at low temperature: WZ structure at 20 K reported in ref 92; WZ elastic constants at 4 K reported in ref 93. Experimental data measured at room temperature (in parentheses): ref 11–16, 92, and 93. [c]Calculated by LS simulations using the SM reported in ref 64. [d]Ref 65. [e]Ref 66. [f]Ref 10, 29, 45, and 46.

effective charges of 1.0, 1.1, and 1.4 e, respectively. As is shown in Figure S1 (Supporting Information), the inverted short-range Zn–O interaction potentials are all repulsive and vary slightly. This shows that the choice of initial charge in the range of 1.0∼1.4 e has a minor influence on the short-range potentials.

The second issue is related to the lattice energy of ZnO. According to eqs 5−7, the lattice energy of ZB−ZnO calculated from the potential model should be consistent with the total energy of ZB−ZnO computed by DFT. We have chosen a simple PCRIM to describe the interatomic two-body interactions in ZnO. The nature of this bond is largely ionic and the electrostatic interactions are dominant. Although a Bader analysis was used to determine the values of the effective ion charges, screening of the electrostatic interaction was omitted and the electron clouds are modeled as point charges in our potential model. These simplifications cause relatively large absolute values of the lattice energies of ZnO solids

calculated using our model compared to the total energies by DFT calculations. The Zn–Zn short-range potential energy as a function of lattice parameter, calculated from eq 7, needs to be shifted 6.0 eV/f.u. downward in order to make it converge to zero at large interatomic distances. This potential model is therefore not able to exactly reproduce the total energy (or the cohesive energy, with a clearer physical meaning) of ZnO. For example, the absolute value of the lattice energy of WZ–ZnO calculated by this potential model is 15.35 eV/f.u., which is two times larger than the cohesive energy calculated by DFT (7.69 eV/f.u.) and that obtained from experiments (7.52 eV/f.u.).[10] The failure to reproduce the cohesive energy of ZnO by this potential model is essentially caused by the choice of the PCRIM that the ions remain charged while being pulled apart from each other. As a consequence, the potential model will not properly describe some other physical properties of ZnO with respect to the expanded interatomic distances, for example, the thermal expansion coefficient, or properties of ZnO in the gas phase. In this work, we aim to develop a simple interaction potential model to describe condensed phases of ZnO. Many physical properties of the condensed phases are determined by the shape of the $E-a$ relation near equilibrium interatomic distances. Therefore, this present model is only suited to the studies of certain physical properties of ZnO in solid phases not at extremely high temperatures (e.g., temperature close to or higher than the melting point). A careful evaluation of the potential model will be provided in section 3.

Before further improvement of the parameter set, we checked the quality of the potential parameters directly derived from the LI method. Several physical properties of ZnO polymorphs were calculated from the potential model with parameters derived by the LI (see the values in Table 2 in curly brackets). This set is already able to accurately reproduce the lattice parameters of WZ–, ZB–, and BCT–ZnO, the elastic properties of WZ–ZnO, and the relative stabilities of the WZ, ZB, and RS phases. However, the equilibrated lattice parameters of RS–ZnO and the relative stability of the HC phase cannot be accurately reproduced. Although the lattice parameters of BCT–ZnO can be quite accurately reproduced, the calculated lattice energy of the BCT phase was even slightly lower than the WZ phase, which contradicted the DFT results.

2.3. Fitting Methodology. The eight-parameter PCRIM obtained from the LI was used as an initial guess in the fitting procedure described below. Since the initial guess from the LI method is considerably reliable, only the relaxed fitting procedure[69] was used to further adjust the parameters. Compared to the conventional fitting procedure, the relaxed fitting procedure is computationally more expensive but a higher quality of fitting is achieved. In the relaxed fitting procedure, the error was defined as the squared residual of the physical properties of the optimized configurations. Empirical fitting based on experimental data and ab initio energy surface fitting based on DFT data were combined and carried out simultaneously in our fitting procedure. The scheme for ab initio energy surface fitting used in this work was slightly different from the conventional ones in which the potential parameters are obtained by fitting to the energies with respect to a sequence of geometries, whereas relaxed fitting is not used. In this work, four ZnO polymorphs (WZ, ZB, RS, and HC) were chosen as energy surfaces, and the relaxed fitting was used. All eight parameters obtained from the LI method, including the effective charge, were set as parameters and were adjusted by fitting the experimental data and the DFT data. The

experimental data include the lattice parameters of WZ–ZnO measured by neutron diffractometry at 20 K[92] and the WZ elastic constants measured at 4 K.[93] The DFT data for the ab initio energy surface fitting include the lattice parameters of the ZnO in the ZB, RS, and HC structures and the energy differences of ZnO in these structures with respect to WZ. It is generally known that DFT–GGA calculations systematically show larger lattice parameters in comparison to experimental data. The lattice parameters of ZB–, RS–, and HC–ZnO from our DFT–GGA calculations were normalized by rescaling their volumes. The scale factor used for the rescaling was the ratio of the volume of WZ–ZnO from our DFT–GGA calculation over that of the experimental result.[92] The ratio c/a from our DFT calculations remained unchanged. Besides the structures used in the fitting procedure, the lattice parameters of other structures (the CsCl and BCT structures) from our DFT calculations were also normalized for validation. These normalized lattice parameters are listed in Table 2 in square brackets and the data used in the fitting procedure are listed in Table 2 in bold. All calculations in the fitting procedure were carried out by GULP.[94]

The final parameters are listed in Table 1. Lastly, we checked if the potential model with the adjusted parameters did significantly change from those derived by the LI method. The potentials of different interatomic interactions as a function of interatomic distance are plotted in Figure 1 for both the parameters obtained from the LI method, and those adjusted by the fitting. The shapes of the interaction potentials calculated with the two parameter sets are very similar. A comparison between the physical properties calculated with the two parameter sets (see Table 2) also reveals the similarities of the interaction potentials before and after the fitting procedure. Obviously, only minor modifications were applied to the potentials by the fitting procedure, which greatly improved the aforementioned deficiencies of the initial guess. The interaction potentials with adjusted parameters are very similar to the initial guess. Therefore, the intrinsic correctness of the ab initio calculations is retained.

3. PHYSICAL PROPERTIES OF ZNO

3.1. Lattice Parameters, Elastic Properties, and Structural Stabilities. The most basic requirement for a potential model is that it should accurately reproduce lattice parameters and elastic properties of the structures that are stable in nature. The elastic properties, including elastic constants and bulk modulus, are related to first-order derivatives of the total free energy with respect to atomic displacements. A potential model should also show considerable accuracy in its description of the high-pressure or metastable phases in order to ensure that related phase transitions and the mechanism are described accurately as well.

We now verify our ZnO potential model by reproducing several physical properties of ZnO in different crystal structures. The physical properties of ZnO in the CsCl and BCT structures are in the "validation" set, as those data were not used in the fitting procedure. Physical properties of ZnO at 0 K were calculated by lattice statics (LS) simulations and physical properties of ZnO at finite temperatures were obtained by MD simulations. LS and MD simulations were performed by GULP[94] and LAMMPS[95] codes, respectively. In the MD simulations, a periodic WZ–ZnO matrix containing 4312 atoms was constructed based on the experimental lattice parameters. The equations of motion were integrated using the

velocity Verlet algorithm with a time step of 1 fs. At 300 K and zero pressure, a MD simulation of 0.5 ns was performed on WZ−ZnO in the isobaric−isothermal (NPT) ensemble, out of which the first 0.1 ns was used for equilibration. The velocities were rescaled to the target temperature during the equilibration. The temperature and the pressure were controlled by a standard Nosé-Hoover thermostat and barostat.[96] The results from the LS simulations at 0 K and MD simulations at 300 K are listed in Table 2, together with available experimental data, DFT calculations, and the results calculated using other potentials. In our DFT calculations, the elastic constants were calculated by applying small strains to the unit cell.[97] As with all other DFT calculations in this work, the GGA approach was used, which is known to underestimate the elastic constants. When comparing with the experimental data, it is clear that our potential model is able to accurately reproduce the crystal structure and the elastic properties of WZ−ZnO. The result of our MD simulation at 300 K indicates a volume of the ZnO unit cell of 47.60 Å^3, a ratio of c/a of 1.598, and a u of 0.3814, while the experimental values[92] are 47.63 Å^3, 1.602, and 0.3819, respectively. For the other phases, because they are not stable in nature, the only possible comparison is with DFT calculations. Special emphasis should be placed on the relative stabilities of two phases: HC and BCT. HC is a possible intermediate phase in the pressure-induced WZ-to-RS phase transition,[35,47] and the BCT structure, which has been directly observed by HRTEM in ZnO nanoislands recently,[98] is predicted to be stable under mild negative pressure.[36,37,45] The lattice parameters of all the high-pressure, meta-stable, or unstable structures in equilibrium calculated by the potential model have good agreement with the normalized DFT results. The potential model also reproduces the correct order of the stabilities of bulk ZnO in the six structures studied: $E_{WZ} < E_{ZB} < E_{BCT} < E_{HC} < E_{RS} < E_{CsCl}$. The calculated lattice energy differences of the ZB, RS, HC, and BCT structures with respect to the WZ structure are in good agreement with DFT calculations (see Table 2). In general, our PCRIM shows higher accuracy in reproducing the lattice parameters and relative stabilities of ZnO polymorphs in comparison with other empirical or semiempirical potential models.[59,63−66] Only the stability of the CsCl structure is underestimated by the potential model (1.816 eV/f.u.) compared to DFT calculations (~1.4 eV/f.u.). However, the inaccurately described stability of the CsCl structure also exists in other ZnO potentials.[59,63−66]

3.2. Phonon Dispersion and DOS. In order to further test the validity and accuracy of our ZnO potential, we have calculated the vibrational properties of WZ−ZnO. WZ−ZnO belongs to the space group $P6_3mc$ (C_{6v}^4). Four atoms in the primitive cell have 12 degrees of freedom, and those at the Brillouin zone center (Γ) can be classified by group theory as $2A_1 + 2B_1 + 2E_1 + 2E_2$, including three acoustic modes $E_1 + A_1$. In all of the optical modes, A_1 and E_2 modes are both Raman and infrared active, E_2 modes are Raman active only, and the B_1 modes are silent modes. Figure 2 shows the calculated phonon dispersion curves in the directions of Γ → A and Γ → M and the normalized partial phonon density of states (DOS). The calculated phonon dispersion curves are in excellent agreement with DFT computations, and with inelastic neutron scattering and Raman data.[33,34] Note that the ABOP model[65] for ZnO (whose functional form does not include the long-range Coulombic interactions) is not able to describe the splitting of the longitudinal and transverse modes (LO−TO splitting). Our calculated partial phonon DOS also shows similar results
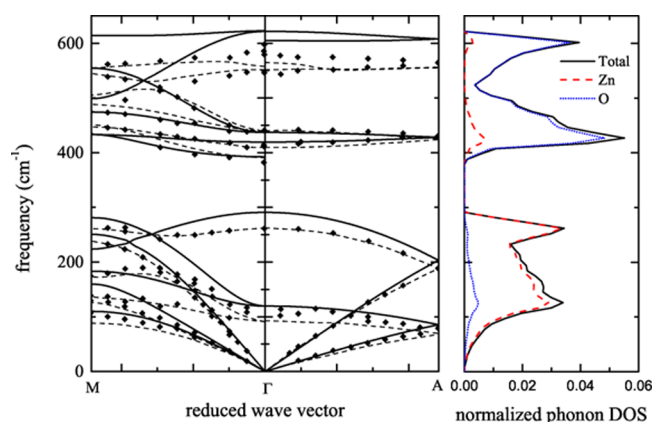

Figure 2. Phonon dispersion (left, solid lines) of WZ−ZnO along Γ−A and Γ−M directions and normalized partial phonon DOS (right) calculated by LD. The experimental data (diamonds) and DFT data (left, dashed lines) are extracted from ref 33.

as previous DFT calculations.[32] The partial phonon DOS indicates that the Zn atoms contribute mostly in the low-frequency phonons and the O atoms contribute mostly in the high-frequency phonons.

3.3. High-Temperature Simulations. Using the same periodic WZ−ZnO model as in the previous MD simulation at 300 K, a direct heating MD simulation was performed in NPT ensemble to test the thermal expansion and melting point for WZ−ZnO. Here, a relatively short time step of 0.5 fs was used. First, the system was equilibrated at 300 K for 1 ns, then the temperature was elevated by 10 K in every 5 ps, from 300 to 3300 K. During heating, the Nosé-Hoover thermostat[96] was used to control the temperature of the system. In Figure 3a, the lattice parameters a and c and the ratio c/a are displayed as a function of temperature. In comparison to experimental results,[99] the linear thermal expansion coefficient obtained from MD simulations is overestimated by a factor of about three. Nonetheless, our MD simulations show correct trends in the changes of a, c, and c/a with increasing temperature. The relative error of the lattice parameters from MD simulations is less than 1% compared with experimental data[99] in the temperature range of 300−1400 K. The melting point from the direct MD simulation was ~2680 K (see Figure 3b), which is higher than that of experimental value[100] of 2242 K. This superheating phenomenon was caused by the finite size effects and the limited simulation time in MD simulations.

To obtain a more accurate melting point for WZ−ZnO from MD simulations, the two-phase method[101] was performed with our ZnO potential model. A simulation box was constructed as a cuboid (2.36 nm × 2.04 nm × 8.70 nm). The c-axis in the WZ structure was oriented along the longest side of the cuboid. Here, we only considered the case that the melting front is perpendicular to the c-axis. In total, the simulation box contained 1536 ZnO pairs. The simulation box was divided into a solid phase region and a liquid phase region, both of which had equal numbers of ZnO pairs. The lattice parameters of WZ−ZnO at 2200 K from MD simulations were used to construct the solid phase. First, the atoms in the solid phase were frozen while the liquid phase was equilibrated at temperatures around 2200 K for 25 ps. Second, the atoms in the solid phase were released and equilibrated together with the liquid phase in the NVE ensemble for 75 ps, where the last 50 ps were used to monitor the solid−liquid interfaces. An
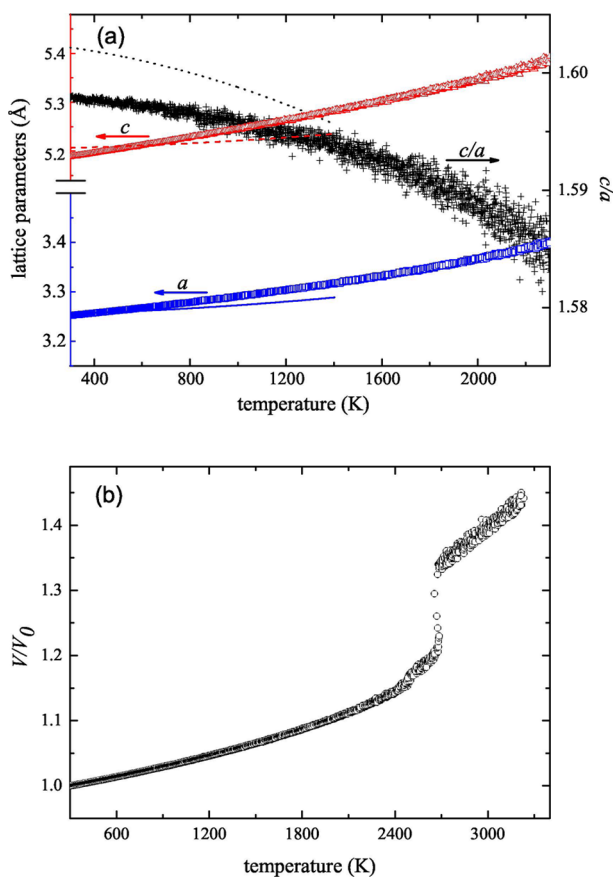
Figure 3. (a) Lattice parameters a (blue squares) and c (red triangles) and the ratio c/a (black crosses) calculated from the MD simulations as a function of temperature compared with experimental data ref 99 (a: the blue solid line; c: the red dashed line; c/a: the black dotted line). (b) Variation of the normalized volume, V/V_0, as a function of temperature from the direct heating MD simulation. The system contained 2156 ZnO pairs, and was annealed from 300 to 3300 K at a constant rate of 10 K/5 ps during the simulation.

equilibrium $P-T$ point was found only if the number of {0001} bilayers in the solid phase remained unchanged during the last 50 ps. Details of simulation methods can be found in refs 101 and 102. We have tried more than 50 initial configurations and equilibrated solid−liquid interfaces were found in nine of them. The melting temperature obtained from the two-phase method is 2308 K, which is in excellent agreement with experimental values.[100]

3.4. High-Pressure Simulations. The pressure-induced WZ-to-RS phase transition in ZnO[10,13−16,28,32,35,39,47,56] and other WZ crystals[87,103−106] is an intriguing phenomenon, whereby the mechanism remains unclear. The HC structure as a possible intermediate phase in the WZ-to-RS phase transition, as predicted by DFT calculations[106] and molecular dynamics simulations,[47,56,103,104] has not yet been found experimentally. However, the HC structure has been reported experimentally only in ZnO: a few layers of local HC structure have been observed at ZnO/Ag boundaries.[107] To have a comparative study of the metastable HC phase, we extended our DFT calculations to three other II−VI semiconductors (ZnS, CdS, and CdSe), whose WZ phase is stable at room temperature and ambient pressure conditions or can be artificially synthesized. Our DFT calculations showed that among these II−VI semiconductors, ZnO has the smallest energy difference

between the HC structure and the WZ structure, $\Delta E_{HC\text{-}WZ}$, and the lowest value of the ratio ρ, where $\rho = \Delta E_{HC\text{-}WZ}/\Delta E_{RS\text{-}WZ}$, at zero temperature, zero pressure conditions. Details about the DFT calculations and the results are provided in the Supporting Information. Among WZ II−VI semiconductors, ZnO may be the best candidate for finding a stabilized HC structure in experiments.

Figure 4 shows the enthalpies of ZnO with WZ, HC, and RS crystal structures as a function of hydrostatic pressure at 0 K.
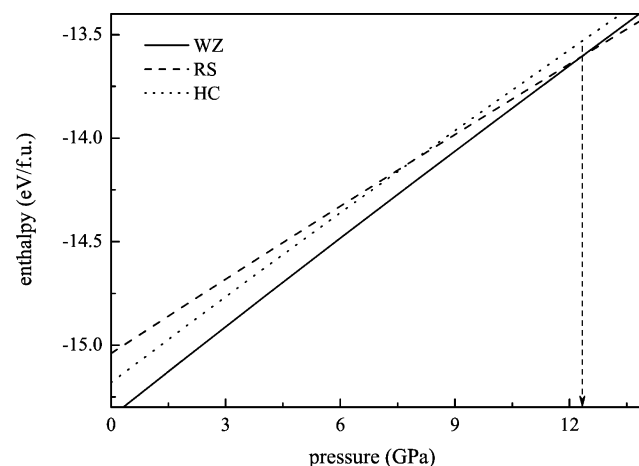

Figure 4. Enthalpies as a function of hydrostatic pressure for ZnO in the WZ (solid line), HC (dotted line), and RS (dashed line) structures. The vertical arrow indicates the pressure of equal enthalpy for the WZ and the RS structures.

Our potential model predicts that the point where the enthalpies of the WZ− and HC−ZnO are equal is 12.3 GPa, which is slightly higher than that reported in experiments[13−16] (8.7−10.5 GPa) and in DFT calculations[10,16,35,39] (6.6−14.5 GPa). The enthalpy of the HC structure never shows a minimum in the studied pressure range, which agrees with previous DFT studies.[28] Therefore, it is unlikely to stabilize the HC structure in ZnO by merely applying hydrostatic pressure.

However, it was predicted by DFT calculations[28] that in a certain pressure range, the enthalpy of HC−ZnO was minimized by applying uniaxial pressure along the c-axis (the WZ ⟨0001⟩ direction). The transition pressure is 6.0 GPa found by means of DFT calculations using the local density approximation (LDA).[28] Using our potential model, the WZ-to-HC transition under uniaxial pressure was tested by means of MD simulations. The same system as in the direct heating MD simulation was used and first equilibrated at 300 K and zero pressure for 2 ns. After equilibration, the temperature was kept constant at 300 K. Uniaxial pressure along the c-axis was applied and increased at a rate of 0.05 GPa/10 ps until the pressure reached 10 GPa. Next, the uniaxial pressure was released at the same rate until it reached zero. During the compression and the reverse process, the pressure in other directions was kept at a value of zero. In Figure 5a, the snapshots of the ZnO matrix clearly indicate the WZ-to-HC phase transition and its reverse transition. By plotting the ratio of c/a as a function of pressure, it is shown in Figure 5c that the WZ-to-HC transition pressure takes place at 8.8 GPa and the reverse transition takes place at 2.9 GPa with a large hysteresis. Based on the previous studies[28] and our MD simulations, the HC structure is very likely to be stabilized by applying uniaxial pressure along the c-axis in WZ−ZnO. If the HC phase can be
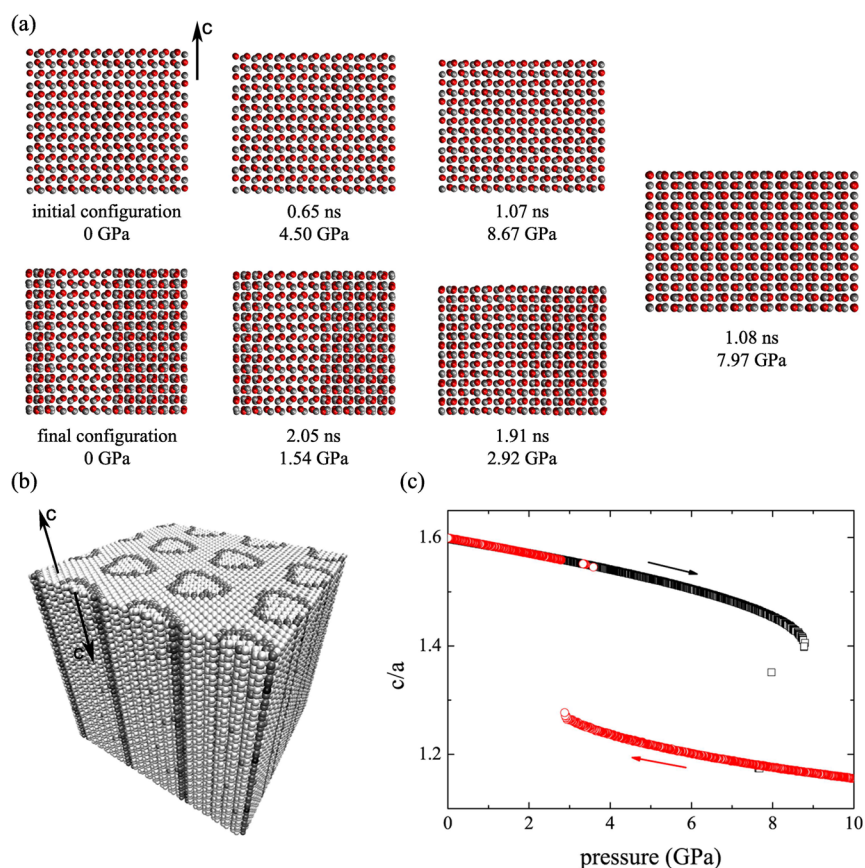
Figure 5. (a) Snapshots of bulk ZnO from MD simulations at 300 K. A uniaxial pressure was applied along the *c*-axis (WZ ⟨0001⟩ direction) and released when it was reached 10 GPa. A WZ-to-HC phase transition was observed under an uniaxial pressure of 8.8 GPa and the reverse transition was observed under 2.9 GPa. The red and black spheres are O and Zn, respectively. (b) A 3 × 3 × 3 matrix shows that BCT−ZnO was formed as boundaries (darker regions) that separate two WZ−ZnO grains (lighter regions) with antiparallel *c*-axes (c) *c/a* as a function of uniaxial pressure from MD simulations. Black squares are the data from upstroke phase transition and the red circles are the data from downstroke reversed phase transition.

stabilized in ZnO or other WZ materials, many interesting phenomena are expected to be observed: the dipole moments in the WZ nanostructures will totally disappear and so does the piezoelectric property in the WZ materials. However, difficulties can be expected in experiments: for bulk materials, a perfect single crystal may be hard to access, as achieving a homogeneous transition in bulk materials is difficult. For mesomaterials or nanomaterials, applying a uniaxial pressure on a single object is difficult.

Another interesting phenomenon found in the MD simulations is that the BCT structure formed in the reverse HC-to-WZ transition (see Figure 5a,b). In Figure 5b, the final configuration of the released unit cell was expanded to a 3 × 3 × 3 matrix and each atom was colored by the number of its nearest neighbors, n_{nn}. Here, the atoms are defined to be the nearest neighbors if their interatomic distance is less than 2.8 Å. In this way, the BCT domains ($n_{nn} = 5$) and the WZ domains ($n_{nn} = 4$) can be easily distinguished. It is clear from Figure 5b that the BCT−ZnO domains formed as boundaries that are separating two WZ−ZnO grains with antiparallel *c*-axes. Recently, there has been much discussion about the BCT structure in ZnO and other binary semiconductors,[36,37,43−45,49,61,62,98] including molecular simulation studies with various ZnO potentials.[45,61,62] Here we note that the SMs derived by Binks et al.[64] and Alsunaidi et al.[58] overestimate the stability of BCT−ZnO. The relative energy differences of the

BCT compared to the WZ (ΔE_{BCT-WZ}) calculated using these potential models[59,64] is about 0.007 eV/f.u., which is very small in comparison to our DFT−GGA results of 0.048 eV/f.u. and previous LDA−GGA results[45] of 0.074 eV/f.u. Therefore, we should strongly question the findings of the BCT−ZnO structure appearing in the molecular simulations as it may be an artifact of the interaction potential model.

3.5. Surface Energy Calculations. If the interaction potentials are to be used in the studies of ZnO nanostructures, the capability of the potentials to reproduce the surface properties of ZnO needs to be tested. Previous studies showed that the nonpolar {10$\bar{1}$0} and {11$\bar{2}$0} surfaces are the most stable surfaces.[108,109] However, the polar ± {0001} surfaces can be stabilized by different mechanisms.[110−114] The surface energies of these four different polar and nonpolar surfaces in WZ−ZnO were calculated by both DFT and the ZnO potential model. In the classical LS simulations, four two-dimensional periodical slab models were constructed, whereby the four different surfaces are oriented in a nonperiodic direction. These slabs were divided into two regions by the middle planes perpendicular to the surface normal. The atoms in the region 1 (surface region) were allowed to relax, while the atoms in region 2 (bulk region) were fixed. The thickness of slabs was at least 20 Å and the surface areas ranged from 402 to 581 Å². It is possible to cut a slab with a {10$\bar{1}$0} surface in two ways: either breaking one bond or two bonds. Only the former case is

considered here since it is most favorable. The $\{11\overline{2}0\}$ surface can only be cut in one way, while there are two ways for the $\pm\{0001\}$, one by breaking one bond, the other by breaking three bonds. Again, only the surface obtained by breaking one bond is considered. In order to stabilize the polar surfaces, "point defects"[115] were constructed by moving a quarter of surface atoms from the surface to the bottoms of the slabs. The surface energies can be calculated as

$$E = \frac{E_{surface} - nE_{bulk}}{A} \qquad (10)$$

where $E_{surface}$ is the energy of all the atoms in the surface region, n is the number of $\{ZnO\}$ pairs in surface region, E_{bulk} is the energy per $\{ZnO\}$ pair in the bulk, and A is the surface area of the simulation cell.

For the DFT calculations, the schemes used to calculate the surface energies are slightly different from those in the classical LS simulations. First, in DFT calculations, 3-D periodic conditions must be used so the vacuum needs to be constructed as a vacuum slab between the ZnO slab surfaces. Large slab models as in the LS simulations exceed the computational limit of DFT calculations. However, to obtain a reliable surface energy, both the slab itself and the vacuum must be sufficiently thick. The thickness of the $\{10\overline{1}0\}$-, $\{11\overline{2}0\}$-, and $\pm\{0001\}$-slabs were 21.22 (16 layers), 19.36 (13 layers), and 29.20 (12 bilayers) Å, respectively, and the thickness of the vacuum layers were ~28 Å. Monkhorst Pack k-meshes[79] of 28 × 17 × 1, 17 × 17 × 1, and 28 × 28 × 1 were used for the $\{10\overline{1}0\}$-, $\{11\overline{2}0\}$-, and $\pm\{0001\}$-slabs, respectively. Second, since the total energy of the slab needs to be compared with the total energy of a bulk cell, only stoichiometric cells can be used. For the $\{10\overline{1}0\}$ and $\{11\overline{2}0\}$ surfaces, this is automatically the case, since each layer contains an equal amount of Zn and O. The $\{0001\}$ surface slab however, consists of bilayers, thus an (unreconstructed) $\{0001\}$-slab always contains one Zn-terminated and one O-terminated surface. Since only the total energy can be calculated, these surfaces cannot be distinguished, and therefore, an average surface energy is obtained.

The relaxed and unrelaxed surface energies of four surfaces are listed in Table 3 and are compared with SMs,[57,116] ReaxFF,[66] and other DFT results.[108−110] Even though PCRIM was used in our ZnO potentials, whereby surface atoms cannot have a different charge than the bulk atoms, the surface energy calculations with the newly developed potentials show considerable agreement with DFT results. The calculations predict the correct relative order of the surface energies for different surfaces: $E_{O\text{-}\{000\overline{1}\}}$ and $E_{Zn\text{-}\{0001\}} > E_{\{11\overline{2}0\}} > E_{\{10\overline{1}0\}}$. However, the surface energies calculated for the nonpolar $\{10\overline{1}0\}$ and $\{11\overline{2}0\}$ surfaces using our ZnO potential model (~1.5 J/m^2) are slightly larger than those obtained from the DFT calculations (0.94~1.4 J/m^2). SMs and ReaxFF shows better capabilities to reproduce the surface energies of nonpolar surfaces of ZnO than the PCRIM.

4. CONCLUSIONS

In summary, two main conclusions can be drawn from our work: first, we have demonstrated that the combination of the LI, empirical, and ab initio energy surfaces fittings is an efficient way to develop new potentials with high intrinsic accuracy. Second, a high-performance set of interatomic pair potentials based on an eight-parameters PCRIM was developed and validated for ZnO. Compared to other SMs, ABOP, or ReaxFF (which have much more parameters and much more complex

Table 3. Relaxed and Unrelaxed (in Parentheses) Surface Energy for Nonpolar and Polar ZnO Surfaces in Comparison with Shell Models (SMs), Reactive Force Field (ReaxFF), and DFT Calculations; The Unit of the Surface Energy is in J/m^2

	force fields			ab initio calculations	
	PCRIM	SM^a	SM^b	ReaxFF^c	this work	literature^d
$\{10\overline{1}0\}$	1.46 (1.60)	1.1	1.003	0.96	0.94 (1.28)	1.04 (1.20), 1.3
$\{11\overline{2}0\}$	1.51 (1.59)	1.2		1.06	0.98 (1.28)	1.06 (1.19), 1.4
Zn-$\{0001\}$	2.00 (2.53)^e	2.1^f			1.90 (2.16)^g	(~2.0)^h
O-$\{000\overline{1}\}$	2.23 (3.04)^e					

^{a}Ref 116. ^{b}Ref 57. ^{c}Ref 66. ^{d}Ref 108−110. ^{e}"Point defects"[115] were constructed on the surfaces in order to remove the dipole moments. ^{f}One-fourth of the surface atoms were removed from both sides of the polar surfaces to stabilized them.[116] The difference in surface energies between the Zn-terminated and O-terminated $\pm\{0001\}$ surfaces can not be distinguished. ^{g}The average of the Zn-terminated and O-terminated $\pm\{0001\}$ surfaces. ^{h}The average of unrelaxed surface energies of the Zn-terminated and O-terminated $\pm\{0001\}$ surfaces, which is derived by the cleavage energy[110] divided by two.

functional forms to describe the interactions), our eight-parameter PCRIM shows similar or even better results in reproducing physical properties of ZnO. These physical properties include the lattice parameters, elastic constants, bulk modulus, structural stabilities, lattice dynamics, and surface energies. The variation of the lattice parameters of WZ−ZnO at high temperature conditions can be quantitatively correctly described by the potential model. The melting point of ZnO was estimated to be 2308 K by the two-phase method, which is in excellent agreement with the experimental result of 2242 K. The coexistence pressure of the WZ and RS phase at 0 K is predicted at 12.3 GPa. A WZ-to-HC transition induced by uniaxial pressure predicted by previous DFT calculations was also reproduced by means of MD simulations with our newly developed ZnO potential model.

Finally, we summarized the shortcomings of our ZnO potential model: (i) The stabilities of the CsCl structures in ZnO are underestimated by this model; (ii) The linear expansion coefficient of WZ−ZnO is overestimated by a factor of 3 when compared with experimental data; (iii) The surface energies calculated for the nonpolar $\{10\overline{1}0\}$ and $\{11\overline{2}0\}$ surfaces are slightly larger than the DFT results.

In this work, we explored a rational and efficient routine to develop pair potentials for a binary compound. There is an urgent need to develop more simple but effective potential models to extend theoretical studies on semiconductor materials, especially for accurate modeling of phase transitions and of large systems. Using our approach, interaction potentials of many other materials could be developed. In particular, our interaction potential model for ZnO is expected to enable reliable studies of the physical properties of ZnO bulk materials and solid−solid phase transitions in ZnO. Surface properties are essential at the nanoscale. Some of the surface energies calculated with this potential model deviate from DFT−GGA results by about 50%. However, differences between DFT results obtained with different schemes (LDA, GGA, B3LYP, and HF) are also large.[109] Whether this potential model is suitable for simulating ZnO nanostructures remains unclear.

We encourage readers to apply our ZnO potential model in the simulation of ZnO nanostructures and to compare the results with first principles calculations or experiments.

■ ASSOCIATED CONTENT

Ⓢ Supporting Information

Figure S1, details of the DFT calculations, and the results of the lattice parameters and relative stabilities of ZnS, CdS, and CdSe in the WZ, HC, and RS structures. This material is available free of charge via the Internet at http://pubs.acs.org.

■ AUTHOR INFORMATION

Corresponding Author

*E-mail: t.j.h.vlugt@tudelft.nl.

Notes

The authors declare no competing financial interest.

■ ACKNOWLEDGMENTS

■ REFERENCES

(1) Özgür, U.; Alivov, Y. I.; Liu, C.; Teke, A.; Reshchikov, M. A.; Doğan, S.; Avrutin, V.; Cho, S.-J.; Morkoç, H. A Comprehensive Review of ZnO Materials and Devices. *J. Appl. Phys.* **2005**, *98*, 041301.

(2) Klingshirn, C. ZnO: From Basics towards Applications. *Phys. Status Solidi B* **2007**, *244*, 3027−3073.

(3) Baruah, S.; Dutta, J. Hydrothermal Growth of ZnO Nanostructures. *Sci. Technol. Adv. Mater.* **2009**, *10*, 013001.

(4) Heo, Y. W.; Norton, D. P.; Tien, L. C.; Kwon, Y.; Kang, B. S.; Ren, F.; Pearton, S. J.; LaRoche, J. R. ZnO Nanowire Growth and Devices. *Mater. Sci. Eng. R* **2004**, *47*, 1−47.

(5) Xu, S.; Wang, Z. L. One-Dimensional ZnO Nanostructures: Solution Growth and Functional Properties. *Nano Res.* **2011**, *4*, 1013−1098.

(6) Lu, J. G.; Chang, P.; Fan, Z. Quasi-One-Dimensional Metal Oxide Materials-Synthesis, Properties and Applications. *Mater. Sci. Eng. R* **2006**, *52*, 49−91.

(7) Sekiguchi, T.; Miyashita, S.; Obara, K.; Shishido, T.; Sakagami, N. Hydrothermal Growth of ZnO Single Crystals and Their Optical Characterization. *J. Cryst. Growth* **2000**, *214−215*, 72−76.

(8) Matsumoto, K.; Noda, K. Crystal Growth of ZnO by Chemical Transport Using HgCl$_2$ as a Transport Agent. *J. Cryst. Growth* **1990**, *102*, 137−140.

(9) Hachigo, A.; Nakahata, H.; Higaki, K.; Fujii, S.; Shikata, S. Heteroepitaxial Growth of ZnO Films on Diamond (111) Plane by Magnetron Sputtering. *Appl. Phys. Lett.* **1994**, *65*, 2556−2558.

(10) Jaffe, J. E.; Snyder, J. A.; Lin, Z.; Hess, A. C. LDA and GGA Calculations for High-Pressure Phase Transitions in ZnO and MgO. *Phys. Rev. B* **2000**, *62*, 1660−1665.

(11) M., A. A. A. B.; Ueta, A.; Avramescu, A.; Kumano, H.; Suemune, I.; Ok, Y.-W.; Seong, T.-Y. Growth and Characterization of Hypothetical Zinc-Blende ZnO Films on GaAs(001) Substrates with ZnS Buffer Layers. *Appl. Phys. Lett.* **2000**, *76*, 550−552.

(12) Kim, S.-K.; Jeong, S.-Y.; Cho, C.-R. Structural Reconstruction of Hexagonal to Cubic ZnO Films on Pt/Ti/SiO$_2$/Si Substrate by Annealing. *Appl. Phys. Lett.* **2003**, *82*, 562−564.

(13) Bates, C. H.; White, W. B.; Roy, R. New High-Pressure Polymorph of Zinc Oxide. *Science* **1962**, *137*, 993.

(14) Gerward, L.; Staun Olsen, J. The High-Pressure Phase of Zincite. *J. Synchrotron Radiat.* **1995**, *2*, 233−235.

(15) Desgreniers, S. High-Density Phases of ZnO: Structural and Compressive Parameters. *Phys. Rev. B* **1998**, *58*, 14102−14105.

(16) Karzel, H.; Potzel, W.; Köfferlein, M.; Schiessl, W.; Steiner, M.; Hiller, U.; Kalvius, G. M.; Mitchell, D. W.; Das, T. P.; Blaha, P.; et al. Lattice Dynamics and Hyperfine Interactions in ZnO and ZnSe at High External Pressures. *Phys. Rev. B* **1996**, *53*, 11425−11438.

(17) Meulenkamp, E. A. Synthesis and Growth of ZnO Nanoparticles. *J. Phys. Chem. B* **1998**, *102*, 5566−5572.

(18) Park, W. I.; Kim, D. H.; Jung, S.-W.; Yi, G.-C. Metalorganic Vapor-Phase Epitaxial Growth of Vertically Well-Aligned ZnO Nanorods. *Appl. Phys. Lett.* **2002**, *80*, 4232−4234.

(19) Huang, M. H.; Mao, S.; Feick, H.; Yan, H.; Wu, Y.; Kind, H.; Weber, E.; Russo, R.; Yang, P. Room-Temperature Ultraviolet Nanowire Nanolasers. *Science* **2001**, *292*, 1897−1899.

(20) Pan, Z. W.; Dai, Z. R.; Wang, Z. L. Nanobelts of Semiconducting Oxides. *Science* **2001**, *291*, 1947−1949.

(21) Gao, P. X.; Ding, Y.; Mai, W.; Hughes, W. L.; Lao, C.; Wang, Z. L. Conversion of Zinc Oxide Nanobelts into Superlattice-Structured Nanohelices. *Science* **2005**, *309*, 1700−1704.

(22) Sun, Y.; Fuge, G. M.; Fox, N. A.; Riley, D. J.; Ashfold, M. N. R. Synthesis of Aligned Arrays of Ultrathin ZnO Nanotubes on a Si Wafer Coated with a Thin ZnO Film. *Adv. Mater.* **2005**, *17*, 2477−2481.

(23) Jung, S.; Cho, W.; Lee, H. J.; Oh, M. Self-Template-Directed Formation of Coordination-Polymer Hexagonal Tubes and Rings, and their Calcination to ZnO Rings. *Angew. Chem., Int. Ed.* **2009**, *48*, 1459−1462.

(24) Yu, W. D.; Li, X. M.; Gao, X. D. Self-Catalytic Synthesis and Photoluminescence of ZnO Nanostructures on ZnO Nanocrystal Substrates. *Appl. Phys. Lett.* **2004**, *84*, 2658−2660.

(25) Djurišić, A. B.; Leung, Y. H.; Choy, W. C. H.; Cheah, K. W.; Chan, W. K. Visible Photoluminescence in ZnO Tetrapod and Multipod Structures. *Appl. Phys. Lett.* **2004**, *84*, 2635−2637.

(26) Zhang, H.; Yang, D.; Ji, Y.; Ma, X.; Xu, J.; Que, D. Low Temperature Synthesis of Flowerlike ZnO Nanostructures by Cetyltrimethylammonium Bromide-Assisted Hydrothermal Process. *J. Phys. Chem. B* **2004**, *108*, 3955−3958.

(27) Wang, Z. L.; Song, J. Piezoelectric Nanogenerators Based on Zinc Oxide Nanowire Arrays. *Science* **2006**, *312*, 242−246.

(28) Sarasamak, K.; Limpijumnong, S.; Lambrecht, W. R. L. Pressure-Dependent Elastic Constants and Sound Velocities of Wurtzite SiC, GaN, InN, ZnO, and CdSe, and Their Relation to the High-Pressure Phase Transition: A First-Principles Study. *Phys. Rev. B* **2010**, *82*, 035201.

(29) Wu, X.; Vanderbilt, D.; Hamann, D. R. Systematic Treatment of Displacements, Strains, and Electric Fields in Density-Functional Perturbation Theory. *Phys. Rev. B* **2005**, *72*, 035105.

(30) Schröer, P.; Krüger, P.; Pollmann, J. First-Principles Calculation of the Electronic Structure of the Wurtzite Semiconductors ZnO and ZnS. *Phys. Rev. B* **1993**, *47*, 6971−6980.

(31) Erhart, P.; Albe, K.; Klein, A. First-Principles Study of Intrinsic Point Defects in ZnO: Role of Band Structure, Volume Relaxation, and Finite-Size Effects. *Phys. Rev. B* **2006**, *73*, 205203.

(32) Seko, A.; Oba, F.; Kuwabara, A.; Tanaka, I. Pressure-Induced Phase Transition in ZnO and ZnO-MgO Pseudobinary System: A First-Principles Lattice Dynamics Study. *Phys. Rev. B* **2005**, *72*, 024107.

(33) Serrano, J.; Manjón, F. J.; Romero, A. H.; Ivanov, A.; Cardona, M.; Lauck, R.; Bosak, A.; Krisch, M. Phonon Dispersion Relations of Zinc Oxide: Inelastic Neutron Scattering and Calculations. *Phys. Rev. B* **2010**, *81*, 174304.

(34) Serrano, J.; Romero, A. H.; Manjón, F. J.; Lauck, R.; Cardona, M.; Rubio, A. Pressure Dependence of the Lattice Dynamics of ZnO: An Ab Initio Approach. *Phys. Rev. B* **2004**, *69*, 094306.

(35) Cai, J.; Chen, N. First-Principles Study of the Wurtzite-to-Rocksalt Phase Transition in Zinc Oxide. *J. Phys.: Condens. Matter* **2007**, *19*, 266207.

(36) Morgan, B. J. First-Principles Study of Epitaxial Strain as a Method of B4 → BCT Stabilization in ZnO, ZnS, and CdS. *Phys. Rev. B* **2010**, *82*, 153408.

(37) Zwijnenburg, M. A.; Illas, F.; Bromley, S. T. Apparent Scarcity of Low-Density Polymorphs of Inorganic Solids. *Phys. Rev. Lett.* **2010**, *104*, 175503.

(38) Schleife, A.; Fuchs, F.; Furthmüller, J.; Bechstedt, F. First-Principles Study of Ground- and Excited-State Properties of Mgo, ZnO, and CdO Polymorphs. *Phys. Rev. B* **2006**, *73*, 245212.

(39) Limpijumnong, S.; Jungthawan, S. First-Principles Study of the Wurtzite-to-Rocksalt Homogeneous Transformation in ZnO: A Case of a Low-Transformation Barrier. *Phys. Rev. B* **2004**, *70*, 054104.

(40) Li, C.; Guo, W.; Kong, Y.; Gao, H. First-Principles Study of the Dependence of Ground-State Structural Properties on the Dimensionality and Size of ZnO Nanostructures. *Phys. Rev. B* **2007**, *76*, 035322.

(41) Topsakal, M.; Cahangirov, S.; Bekaroglu, E.; Ciraci, S. First-Principles Study of Zinc Oxide Honeycomb Structures. *Phys. Rev. B* **2009**, *80*, 235119.

(42) Li, Z.; Xu, Y.; Gao, G.; Cui, T.; Ma, Y. Tetragonal High-Pressure Phase of ZnO Predicted From First Principles. *Phys. Rev. B* **2009**, *79*, 193201.

(43) Morgan, B. J. Preferential Stability of the d-BCT Phase in ZnO Thin Films. *Phys. Rev. B* **2009**, *80*, 174105.

(44) Agrawal, R.; Paci, J. T.; Espinosa, H. D. Large-Scale Density Functional Theory Investigation of Failure Modes in ZnO Nanowires. *Nano Lett.* **2010**, *10*, 3432−3438.

(45) Wang, J.; Kulkarni, A. J.; Sarasamak, K.; Limpijumnong, S.; Ke, F. J.; Zhou, M. Molecular Dynamics and Density Functional Studies of a Body-Centered-Tetragonal Polymorph of ZnO. *Phys. Rev. B* **2007**, *76*, 172103.

(46) Carrasco, J.; Illas, F.; Bromley, S. T. Ultralow-Density Nanocage-Based Metal-Oxide Polymorphs. *Phys. Rev. Lett.* **2007**, *99*, 235502.

(47) Boulfelfel, S. E.; Leoni, S. Competing Intermediates in the Pressure-Induced Wurtzite to Rocksalt Phase Transition in ZnO. *Phys. Rev. B* **2008**, *78*, 125204.

(48) Kubo, M.; Oumi, Y.; Takaba, H.; Chatterjee, A.; Miyamoto, A.; Kawasaki, M.; Yoshimoto, M.; Koinuma, H. Homoepitaxial Growth Mechanism of ZnO(0001): Molecular-Dynamics Simulations. *Phys. Rev. B* **2000**, *61*, 16187−16192.

(49) Kulkarni, A. J.; Zhou, M.; Sarasamak, K.; Limpijumnong, S. Novel Phase Transformation in ZnO Nanowires under Tensile Loading. *Phys. Rev. Lett.* **2006**, *97*, 105502.

(50) Combe, N.; Chassaing, P.-M.; Demangeot, F. Surface Effects in Zinc Oxide Nanoparticles. *Phys. Rev. B* **2009**, *79*, 045408.

(51) Raymand, D.; van Duin, A. C. T.; Spångberg, D.; Goddard, W. A., III; Hermansson, K. Water Adsorption on Stepped ZnO Surfaces from MD Simulation. *Surf. Sci.* **2010**, *604*, 741−752.

(52) Raymand, D.; Jacobsson, T. J.; Hermansson, K.; Edvinsson, T. Investigation of Vibrational Modes and Phonon Density of States in ZnO Quantum Dots. *J. Phys. Chem. C* **2012**, *116*, 6893−6901.

(53) Momeni, K.; Odegard, G. M.; Yassar, R. S. Finite Size Effect on the Piezoelectric Properties of ZnO Nanobelts: A Molecular Dynamics Approach. *Acta Mater.* **2012**, *60*, 5117−5124.

(54) Kulkarni, A. J.; Zhou, M.; Ke, F. J. Orientation and Size Dependence of the Elastic Properties of Zinc Oxide Nanobelts. *Nanotechnology* **2005**, *16*, 2749.

(55) Dai, L.; Cheong, W. C. D.; Sow, C. H.; Lim, C. T.; Tan, V. B. C. Molecular Dynamics Simulation of ZnO Nanowires: Size Effects, Defects, and Super Ductility. *Langmuir* **2010**, *26*, 1165−1171.

(56) Dong, X.; Liu, F.; Xie, Y.; Shi, W.; Ye, X.; Jiang, J. Z. Pressure-Induced Structural Transition of ZnO Nanocrystals Studied with Molecular Dynamics. *Comput. Mater. Sci.* **2012**, *65*, 450−455.

(57) Whitmore, L.; Sokol, A. A.; Catlow, C. R. A. Surface Structure of Zinc Oxide (1010), Using an Atomistic, Semi-Infinite Treatment. *Surf. Sci.* **2002**, *498*, 135−146.

(58) Al-Sunaidi, A. A.; Sokol, A. A.; Catlow, C. R. A.; Woodley, S. M. Structures of Zinc Oxide Nanoclusters: As Found by Revolutionary Algorithm Techniques. *J. Phys. Chem. C* **2008**, *112*, 18860−18875.

(59) Catlow, C. R. A.; French, S. A.; Sokol, A. A.; Al-Sunaidi, A. A.; Woodley, S. M. Zinc Oxide: A Case Study in Contemporary Computational Solid State Chemistry. *J. Comput. Chem.* **2008**, *29*, 2234−2249.

(60) Agrawal, R.; Peng, B.; Gdoutos, E. E.; Espinosa, H. D. Elasticity Size Effects in ZnO Nanowires: A Combined Experimental-Computational Approach. *Nano Lett.* **2008**, *8*, 3668−3674.

(61) Agrawal, R.; Peng, B.; Espinosa, H. D. Experimental-Computational Investigation of ZnO Nanowires Strength and Fracture. *Nano Lett.* **2009**, *9*, 4177−4183.

(62) Demiroglu, I.; Bromley, S. T. Nanofilm versus Bulk Polymorphism in Wurtzite Materials. *Phys. Rev. Lett.* **2013**, *110*, 245501.

(63) Lewis, G. V.; Catlow, C. R. A. Potential Models for Ionic Oxides. *J. Phys. C: Solid State Phys.* **1985**, *18*, 1149.

(64) Binks, D. J.; Grimes, R. W. Incorporation of Monovalent Ions in ZnO and Their Influence on Varistor Degradation. *J. Am. Ceram. Soc.* **1993**, *76*, 2370−2372.

(65) Erhart, P.; Juslin, N.; Goy, O.; Nordlund, K.; Müller, R.; Albe, K. Analytic Bond-Order Potential for Atomistic Simulations of Zinc Oxide. *J. Phys.: Condens. Matter* **2006**, *18*, 6585.

(66) Raymand, D.; van Duin, A. C. T.; Baudin, M.; Hermansson, K. A Reactive Force Field (ReaxFF) for Zinc Oxide. *Surf. Sci.* **2008**, *602*, 1020−1031.

(67) Larsson, H. R.; van Duin, A. C. T.; Hartke, B. Global Optimization of Parameters in the Reactive Force Field ReaxFF for SiOH. *J. Comput. Chem.* **2013**, *34*, 2178−2189.

(68) Iype, E.; Hütter, M.; Jansen, A. P. J.; Nedea, S. V.; Rindt, C. C. M. Parameterization of a Reactive Force Field Using a Monte Carlo Algorithm. *J. Comput. Chem.* **2013**, *34*, 1143−1154.

(69) Gale, J. D. Empirical Potential Derivation for Ionic Materials. *Philos. Mag. B* **1996**, *73*, 3−19.

(70) Chen, N. X. Modified Möbius Inverse Formula and Its Applications in Physics. *Phys. Rev. Lett.* **1990**, *64*, 1193−1195.

(71) Yuan, X.; Chen, N.; Shen, J.; Hu, W. Embedded-Atom-Method Interatomic Potentials from Lattice Inversion. *J. Phys.: Condens. Matter* **2010**, *22*, 375503.

(72) Kang, Y.; Chen, N. Site Preference and Vibrational Properties of ScCu_xAl_12−x. *J. Alloys Compd.* **2003**, *349*, 41−48.

(73) Zhang, S.; Chen, N. Ab Initio Interionic Potentials for NaCl by Multiple Lattice Inversion. *Phys. Rev. B* **2002**, *66*, 064106.

(74) Zhang, S.; Chen, N. Lattice Inversion for Interatomic Potentials in AlN, GaN, and InN. *Chem. Phys.* **2005**, *309*, 309−321.

(75) Tsuneyuki, S.; Tsukada, M.; Aoki, H.; Matsui, Y. First-Principles Interatomic Potential of Silica Applied to Molecular Dynamics. *Phys. Rev. Lett.* **1988**, *61*, 869−872.

(76) Kresse, G.; Furthmüller, J. Efficiency of Ab Initio Total Energy Calculations for Metals and Semiconductors Using a Plane-Wave Basis Set. *Comput. Mater. Sci.* **1996**, *6*, 15−50.

(77) Blöchl, P. E. Projector Augmented-Wave Method. *Phys. Rev. B* **1994**, *50*, 17953−17979.

(78) Perdew, J. P.; Burke, K.; Ernzerhof, M. Generalized Gradient Approximation Made Simple. *Phys. Rev. Lett.* **1996**, *77*, 3865−3868.

(79) Monkhorst, H. J.; Pack, J. D. Special Points for Brillouin-Zone Integrations. *Phys. Rev. B* **1976**, *13*, 5188−5192.

(80) Bader, R. F. W. *Atoms in Molecules: A Quantum Theory*; Oxford University Press: Oxford, 1990.

(81) Tang, W.; Sanville, E.; Henkelman, G. A Grid-Based Bader Analysis Algorithm without Lattice Bias. *J. Phys.: Condens. Matter* **2009**, *21*, 08420.

(82) Sanville, E.; Kenny, S. D.; Smith, R.; Henkelman, G. Improved Grid-based Algorithm for Bader Charge Allocation. *J. Comput. Chem.* **2007**, *28*, 899−908.

(83) Henkelman, G.; Arnaldsson, A.; Jónsson, H. A Fast and Robust Algorithm for Bader Decomposition of Charge Density. *Comput. Mater. Sci.* **2006**, *36*, 354−360.

(84) Rabani, E. An Interatomic Pair Potential for Cadmium Selenide. *J. Chem. Phys.* **2002**, *116*, 258−262.

(85) Schapotschnikow, P.; van Huis, M. A.; Zandbergen, H. W.; Vanmaekelbergh, D.; Vlugt, T. J. H. Morphological Transformations

and Fusion of PbSe Nanocrystals Studied Using Atomistic Simulations. *Nano Lett.* **2010**, *10*, 3966–3971.

(86) Grünwald, M.; Zayak, A.; Neaton, J. B.; Geissler, P. L.; Rabani, E. Transferable Pair Potentials for CdS and ZnS Crystals. *J. Chem. Phys.* **2012**, *136*, 234111.

(87) Wilson, M.; Madden, P. A. Transformations between Tetrahedrally and Octahedrally Coordinated Crystals. *J. Phys.: Condens. Matter* **2002**, *14*, 4629.

(88) Born, M.; E., M. J. Zur Gittertheorie der Ionenkristalle. *Z. Phys.* **1932**, *75*, 1–18.

(89) Morse, P. M. Diatomic Molecules According to the Wave Mechanics. II. Vibrational Levels. *Phys. Rev.* **1929**, *34*, 57–64.

(90) Ewald, P. P. Die Berechnung Optischer und Elektrostatischer Gitterpotentiale. *Ann. Phys* **1921**, *369*, 253–287.

(91) Frenkel, D.; Smit, B. *Understanding Molecular Simulation*, 2nd ed.; Academic Press: New York, 2002.

(92) Albertsson, J.; Abrahams, S. C.; Kvick, A. Atomic Displacement, Anharmonic Thermal Vibration, Expansivity and Pyroelectric Co-efficient Thermal Dependences in ZnO. *Acta Crystallogr., Sect. B* **1989**, *45*, 34–40.

(93) Kobiakov, I. B. Elastic, Piezoelectric and Dielectric Properties of ZnO and CdS Single Crystals in a Wide Range of Temperatures. *Solid State Commun.* **1980**, *35*, 305–310.

(94) Gale, J. D.; Rohl, A. L. The General Utility Lattice Program (GULP). *Mol. Simul.* **2003**, *29*, 291–341.

(95) Plimpton, S. Fast Parallel Algorithms for Short-Range Molecular Dynamics. *J. Comput. Phys.* **1995**, *117*, 1–19.

(96) Martyna, G. J.; Tobias, D. J.; Klein, M. L. Constant Pressure Molecular Dynamics Algorithms. *J. Comput. Phys.* **1994**, *101*, 4177–4189.

(97) Steinle-Neumann, G.; Stixrude, L.; Cohen, R. E. First-Principles Elastic Constants for the HCP Transition Metals Fe, Co, and Re at High Pressure. *Phys. Rev. B* **1999**, *60*, 791–799.

(98) He, M.-R.; Yu, R.; Zhu, J. Reversible Wurtzite-Tetragonal Reconstruction in ZnO(10$\bar{1}$0) Surfaces. *Angew. Chem.* **2012**, *124*, 7864–7867.

(99) Iwanaga, H.; Kunishige, A.; Takeuchi, S. Anisotropic Thermal Expansion in Wurtzite-Type Crystals. *J. Mater. Sci.* **2000**, *35*, 2451–2454.

(100) Lamoreaux, R. H.; Hildenbrand, D. L.; Brewer, L. High-Temperature Vaporization Behavior of Oxides II. Oxides of Be, Mg, Ca, Sr, Ba, B, Al, Ga, In, Tl, Si, Ge, Sn, Pb, Zn, Cd, and Hg. *J. Phys. Chem. Ref. Data* **1987**, *16*, 419–443.

(101) Morris, J. R.; Wang, C. Z.; Ho, K. M.; Chan, C. T. Melting Line of Aluminum from Simulations of Coexisting Phases. *Phys. Rev. B* **1994**, *49*, 3109–3115.

(102) Starikov, S. V.; Stegailov, V. V. Atomistic Simulation of the Premelting of Iron and Aluminum: Implications for High-Pressure Melting-Curve Measurements. *Phys. Rev. B* **2009**, *80*, 220104.

(103) Zahn, D.; Grin, Y.; Leoni, S. Mechanism of the Pressure-Induced Wurtzite to Rocksalt Transition of CdSe. *Phys. Rev. B* **2005**, *72*, 064110.

(104) Grünwald, M.; Rabani, E.; Dellago, C. Mechanisms of the Wurtzite to Rocksalt Transformation in CdSe Nanocrystals. *Phys. Rev. Lett.* **2006**, *96*, 255701.

(105) Knudson, M. D.; Gupta, Y. M.; Kunz, A. B. Transformation Mechanism for the Pressure-Induced Phase Transition in Shocked CdS. *Phys. Rev. B* **1999**, *59*, 11704–11715.

(106) Limpijumnong, S.; Lambrecht, W. R. L. Homogeneous Strain Deformation Path for the Wurtzite to Rocksalt High-Pressure Phase Transition in GaN. *Phys. Rev. Lett.* **2001**, *86*, 91–94.

(107) Tusche, C.; Meyerheim, H. L.; Kirschner, J. Observation of Depolarized ZnO(0001) Monolayers: Formation of Unreconstructed Planar Sheets. *Phys. Rev. Lett.* **2007**, *99*, 026102.

(108) Marana, N. L.; Longo, V. M.; Longo, E.; Martins, J. B. L.; Sambrano, J. R. Electronic and Structural Properties of the (1010) and (1120) ZnO Surfaces. *J. Phys. Chem. A* **2008**, *112*, 8958–8963.

(109) Spencer, M. J. S.; Wong, K. W. J.; Yarovsky, I. Density Functional Theory Modelling of ZnO(10$\bar{1}$0) and ZnO(2$\bar{1}$$\bar{1}$0)

Surfaces: Structure, Properties, and Adsorption of N_2O. *Mater. Chem. Phys.* **2010**, *119*, 505–514.

(110) Wander, A.; Schedin, F.; Steadman, P.; Norris, A.; McGrath, R.; Turner, T. S.; Thornton, G.; Harrison, N. M. Stability of Polar Oxide Surfaces. *Phys. Rev. Lett.* **2001**, *86*, 3811–3814.

(111) Lauritsen, J. V.; Porsgaard, S.; Rasmussen, M. K.; Jensen, M. C. R.; Bechstein, R.; Meinander, K.; Clausen, B. S.; Helveg, S.; Wahl, R.; Kresse, G.; Besenbacher, F. Stabilization Principles for Polar Surfaces of ZnO. *ACS Nano* **2011**, *5*, 5987–5994.

(112) Dulub, O.; Diebold, U.; Kresse, G. Novel Stabilization Mechanism on Polar Surfaces: ZnO(0001)-Zn. *Phys. Rev. Lett.* **2003**, *90*, 016102.

(113) Kresse, G.; Dulub, O.; Diebold, U. Competing Stabilization Mechanism for the Polar ZnO(0001)-Zn Surface. *Phys. Rev. B* **2003**, *68*, 245409.

(114) Kunat, M.; Girol, S. G.; Becker, T.; Burghaus, U.; Wöll, C. Stability of the Polar Surfaces of ZnO: A Reinvestigation Using He-Atom Scattering. *Phys. Rev. B* **2002**, *66*, 081402.

(115) Hamad, S.; Cristol, S.; Catlow, C. R. A. Surface Structures and Crystal Morphology of ZnS: A Computational Study. *J. Phys. Chem. B* **2002**, *106*, 11002–11008.

(116) Nyberg, M.; Nygren, M. A.; Pettersson, L. G. M.; Gay, D. H.; Rohl, A. L. Hydrogen Dissociation on Reconstructed ZnO Surfaces. *J. Phys. Chem.* **1996**, *100*, 9054–9063.